

EVIDENCE FOR NON-EVOLVING Fe II/Mg II RATIOS IN RAPIDLY ACCRETING $Z \sim 6$ QSOS

G. DE ROSA¹, R. DECARLI¹, F. WALTER¹, X. FAN², L. JIANG², J. KURK³, A. PASQUALI⁴, H.-W. RIX¹

ApJ accepted 2011 June 23

ABSTRACT

Quasars (QSOs) at the highest known redshift ($z \sim 6$) are unique probes of the early growth of supermassive black holes (BHs). Until now, only the most luminous QSOs have been studied, often one object at a time. Here we present the most extensive consistent analysis to date of $z > 4$ QSOs with observed NIR spectra, combining three new $z \sim 6$ objects from our ongoing VLT-ISAAC program with nineteen $4 < z < 6.5$ sources from the literature. The new sources extend the existing SDSS sample towards the faint end of the QSO luminosity function. Using a maximum likelihood fitting routine optimized for our spectral decomposition, we estimate the black hole mass (M_{BH}), the Eddington ratio (defined as $L_{\text{bol}}/L_{\text{Edd}}$) and the Fe II/Mg II line ratio, a proxy for the chemical abundance, to characterize both the central object and the broad line region gas. The QSOs in our sample host BHs with masses of $\sim 10^9 M_{\odot}$ that are accreting close to the Eddington luminosity, consistent with earlier results. We find that the distribution of observed Eddington ratios is significantly different than that of a luminosity-matched comparison sample of SDSS QSOs at lower redshift ($0.35 < z < 2.25$): the average $\langle \log(L_{\text{bol}}/L_{\text{Edd}}) \rangle = -0.37$ ($L_{\text{bol}}/L_{\text{Edd}} \sim 0.43$) with a scatter of 0.20 dex for the $z > 4$ sample and the $\langle \log(L_{\text{bol}}/L_{\text{Edd}}) \rangle = -0.80$ ($L_{\text{bol}}/L_{\text{Edd}} \sim 0.16$) with a scatter of 0.24 dex for the $0.35 < z < 2.25$ sample. This implies that, at a given luminosity, the M_{BH} at high- z is typically lower than the average M_{BH} of the lower-redshift population, i.e. the $z > 4$ sources are accreting significantly faster than the lower-redshift ones. We show that the derived Fe II/Mg II ratios depend sensitively on the performed analysis: our self-consistent, homogeneous analysis significantly reduces the Fe II/Mg II scatter found in previous studies. The measured Fe II/Mg II line ratios show no sign of evolution with cosmic time in the redshift range $4 < z < 6.5$. If the Fe II/Mg II line ratio is used as a secondary proxy of the Fe/Mg abundance ratio, this implies that the QSOs in our sample have undergone a major episode of Fe enrichment in the few 100 Myr preceding the cosmic age at which they are observed.

Subject headings: cosmology: observations – quasars: general, emission lines – galaxies: active, high-redshift, formation

1. INTRODUCTION

In the past 10 years, more than 50 QSOs at $z > 5.7$ have been discovered (Fan et al. 2000, 2001, 2003, 2004, 2006; Jiang et al. 2008, 2009; Willott et al. 2007, 2010) thanks to the Sloan Digital Sky Survey (SDSS, York et al. 2000) and other large multi-wavelength surveys such as the Canada France High- z Quasar Survey (CFHQS, Willott et al. 2007). These high-redshift QSOs are among the most luminous sources known to date and are direct probes of the universe less than 1 Gyr after the Big Bang. They are fundamental force studying the early growth of supermassive BHs, galaxy formation and interstellar medium chemical evolution (e.g. Kauffmann & Haenelt 2000; Wyithe & Loeb 2003; Hopkins et al. 2005). Strong emission features excited by the central engine and its immediate surroundings can be used to infer properties of the powering BH and of the circumnuclear gas. For example, measuring the emission line width one can obtain information about the bulk motion of the broad-line region (BLR) gas, that can then

be used to estimate the BH mass (M_{BH}). From the line flux ratios we can instead derive chemical abundances of the BLR gas that are fundamental to set constraints on the star formation history of the QSO host galaxy.

Under the assumption that the dynamics of the BLR is dominated by the central gravitational field, it is possible to estimate M_{BH} by using the velocity and the distance of the line-emitting gas from the central BH: $M_{\text{BH}} \propto R v^2$. From reverberation mapping studies of local active galactic nuclei (AGNs) it has been found that R is related to the continuum luminosity L ($R - L$ relation, e.g. Kaspi et al. 2000): $R \propto L^{0.5}$. Measurements of the luminosity and of the gas velocity, via Doppler-broadened line-width, can thus be used to determine the M_{BH} from single epoch spectra. Various strong emission lines can be used as M_{BH} estimators: H α , H β , Mg II, C IV (for a review on the single-epoch spectrum method see Peterson 2010). For objects in the local universe, the $R - L$ relation and its intrinsic scatter have been investigated in detail using the H β line and the relative continuum. These studies have shown that one can obtain accurate M_{BH} estimates via the H β line. For sources at high- z a complication is that the H β emission line is redshifted out of the visible window already at modest redshifts. Whether or not a particular UV line can be used to estimate M_{BH} depends on how well the respective UV line widths in AGN spectra are correlated. In the case of Mg II Shen et al. (2008), using a large collec-

¹ Max-Planck-Institut für Astronomie Königstuhl 17, D-69117, Heidelberg

² Steward Observatory, University of Arizona, 933 North Cherry Avenue, Tucson, AZ 85721

³ Max-Planck-Institut für Extraterrestrische Physik, Gießenbachstraße 1, 85748, Garching

⁴ Astronomisches Rechen-Institut, Mönchhofstr. 12-14, D-69120, Heidelberg

tion of SDSS spectra, found that $\log ([\text{FWHM}(\text{H}\beta)] / [\text{FWHM}(\text{Mg II})]) = 0.0062$, with a scatter of only 0.11 dex, suggesting that the Mg II can be used as a proxy for the H β line, and thus for the BH mass. On the other hand, the accuracy achievable in the determination of the BH mass from the C IV line remains somewhat controversial, since C IV is a resonance line and absorptions are often detected in its blue wing due to outflows, which in turn affects the line width. With the single-epoch spectrum method it has been possible to estimate the M_{BH} for $z \sim 6$ QSOs (Barth et al. 2003; Willott et al. 2003; Jiang et al. 2007; Kurk et al. 2007, 2009; Willott et al. 2010). These studies have shown that these high- z sources from SDSS host BHs with $M_{\text{BH}} \sim 10^9 M_{\odot}$ and are accreting close to the Eddington limit ($L_{\text{bol}}/L_{\text{Edd}} \sim 1$). However, the $z \sim 6$ QSOs from SDSS only account for the brightest end of the QSO luminosity function. Only few faint QSOs ($z'_{\text{AB}} > 20$) have measured M_{BH} to date: two from the SDSS deep Stripe 82 (Jiang et al. 2008, 2009; Kurk et al. 2007, 2009), a deep imaging survey obtained by repeatedly scanning a stripe (260 deg²) along the celestial equator, and nine from CFHQS (Willott et al. 2010). These sources are powered by less massive BHs (down to $M_{\text{BH}} \sim 10^8 M_{\odot}$) that also appear to accrete close to the Eddington limit. For QSOs at lower redshifts Shen et al. (2008) found that the most luminous QSOs ($L_{\text{bol}} > 10^{47}$ erg s⁻¹) at redshift $2 < z < 3$ are characterized by an Eddington ratio of only $L_{\text{bol}}/L_{\text{Edd}} \sim 0.25$ with a dispersion of 0.23 dex. It seems therefore that high-redshift QSOs have fundamentally different properties than the lower-redshift ones.

Regarding the chemical enrichment, photoionization models show that various emission line ratios are good estimators for the metallicity of the BLR gas (e.g. Hamann et al. 2002; Nagao et al. 2006). It is possible to estimate the BLR gas metallicity and to set constraints on the BLR enrichment history through measurements of the relative abundances of nitrogen (N) respect to carbon (C) and helium (He), since these three elements are formed by different astrophysical processes and on different timescales (Hamann & Ferland 1993): C is rapidly produced in the explosion of massive stars; N is a second generation element, i.e. slowly produced in stars from previously synthesized C and O; He is a primordial element and its abundance does not change significantly with cosmic time. Using these element ratios Jiang et al. (2007) estimated the BLR metallicity for a sample of six luminous QSOs with $5.8 < z < 6.3$, finding super solar metallicities with a typical value of $\sim 4 Z_{\odot}$ and no strong evolution up to $z \sim 6$.

The abundance of Fe and α elements (e.g. O, Mg, Ne that are produced in the stars via α processes) is of particular interest for understanding the chemical evolution of galaxies at high- z . Most of Fe in the solar neighborhoods has been produced via the explosion of type Ia supernovae (SNe Ia) while α elements such as Mg and O are mainly produced by core collapse supernovae (SNe of types II, Ib and Ic). SNe Ia are thought to originate from intermediate-mass stars in close binary systems, characterized by long life-times, while core collapse SNe come from more massive stars which explode very soon after the initial starburst. A time delay between α elements and the Fe enrichment is thus expected. This delay de-

pends on the Initial Mass Function (IMF) and on the galactic star formation history, and can vary from 0.3 Gyr, for massive elliptical galaxies, to 1-3 Gyr, for Milky-Way type galaxies (Matteucci & Recchi 2003). In this picture the Fe/ α ratio is expected to be a strong function of age in young systems. The observational proxy that is usually adopted to trace the Fe/Mg abundance ratio for the BLR gas is the Fe II/Mg II line ratio. Unfortunately this line ratio is only a second order proxy, since it depends not only on the actual abundance of Fe but also significantly on the excitation conditions that determine how strongly Fe II lines are emitted (Baldwin et al. 2004). However, even though to date no calibration is available to convert the observed relative line strengths into actual abundance ratios, the study of the Fe II/Mg II line ratio as a function of look-back time does in itself carry significant information about the BLR chemical enrichment history.

For $z > 5.7$ QSOs the Fe II and the Mg II lines are redshifted into the near-infrared (NIR). Numerous NIR-spectroscopy studies of QSO samples including $z \sim 6$ sources have been carried out in the past (e.g. Maiolino et al. 2001, 2003; Pentericci et al. 2002; Iwamuro et al. 2002, 2004; Barth et al. 2003; Dietrich et al. 2003; Freudling et al. 2003; Willott et al. 2003; Jiang et al. 2007; Kurk et al. 2007, 2009). Their results show an increase in the scatter of the measured Fe II/Mg II line ratios as a function of the redshift. One possible way to interpret the increase in the scatter is that some objects are observed such a short time after the initial starburst that the BLR is not yet fully enriched with Fe (Iwamuro et al. 2004). Nonetheless, several possible systematics related to the adopted fitting procedure could potentially be the cause for the observed discrepancies between different authors: the iron template employed, the wavelength limits over which the template is integrated, the wavelength range over which the template is actually fitted and the wavelength coverage and S/N of the spectra used.

The goal of this paper is to study BH masses, Eddington ratios and to characterize the Fe II and Mg II emission in a large sample of high- z QSOs, by fitting their respective NIR spectra in a coherent and homogeneous way. With the aim of extending the existing SDSS sample of $z \sim 6$ QSOs towards the faint end of the QSO luminosity function, we observed three additional $z \sim 6$ sources (discovery papers: Jiang et al. 2008, De Rosa et al. in prep) with ISAAC (Infrared Spectrometer And Array Camera) mounted on the Very Large Telescope (VLT). The three targets have $19.6 < z'_{\text{AB}} < 20.7$ and have been selected from the SDSS and the SDSS Stripe 82. The observed NIR spectra include the Mg II and Fe II emission lines. We have also collected literature spectra of $z > 4$ QSOs covering the restframe wavelengths between $2700 \text{ \AA} < \lambda < 3200 \text{ \AA}$, characterized by the presence of the Mg II line doublet ($\lambda = 2796, 2803 \text{ \AA}$) and of the Fe II line forest.

The paper is structured as follows. In § 2 we describe the sample, the new observations and the data reduction we have performed. In § 3 the spectral decomposition and the fitting procedure adopted are explained together with their results. In § 4 we estimate the M_{BH} and the Fe II/Mg II line ratio and we discuss their implications.

Finally, we give a brief summary in § 5. We assume the following Λ CDM cosmology throughout the paper: $H_0 = 70 \text{ km s}^{-1} \text{ Mpc}^{-1}$, $\Omega_M = 0.3$, and $\Omega_\Lambda = 0.7$ (Spergel et al. 2007).

2. SAMPLE, OBSERVATIONS AND DATA REDUCTION

Our sample is composed of 22 targets: 3 new spectra observed with VLT-ISAAC (see Tab. 1) and 19 sources from the literature (see Tab. 2), kindly provided by the respective authors. Ten of the literature sources have redshift $4.50 < z < 5.70$ (Iwamuro et al. 2002), while the remaining 9 have $5.70 < z < 6.43$ and z-band magnitudes $z'_{AB} < 20.9$ (magnitudes are taken from the discovery papers).

2.1. New data

We have observed 3 SDSS QSOs with magnitudes $19.6 < z'_{AB} < 20.7$ and redshifts $6.05 < z < 6.08$ (see Tab. 1). The two faintest ones have been selected from the SDSS Stripe 82 and extend the existing sample towards the faint end of the QSO luminosity function. The observations were carried out with ISAAC on Antu (VLT-UT1) in low resolution mode (LR), using the 1024x1024 Hawaii Rockwell array of the Short Wavelength arm. For each QSO the MgII line and the FeII complex were observed: given the redshift of the sources, these features fall in the K band. The selected slit had a width of 1" and combined with the order selection filter it gives a spectral resolution $\lambda/\Delta\lambda \sim 450$. Table 1 summarizes the exposure time for each object. For each observation block (OB), sixteen frames of 148 seconds were taken following an ABBA dithering pattern (with large offsets among the dithered positions: from 20" to 30"). Further, small random offsets within a box of 4" to 18" were applied at each dithered position in order to avoid pixel-related artifacts (jittering). Given the faintness of the sources, the observation setup was chosen so that a bright star was always in the slit, in order to allow a correct centering of the target.

The QSO SDSS J2054-0005 has been discovered in the SDSS deep Stripe 82 by Jiang et al. (2008). Our new ISAAC spectrum confirms the weak-line nature of this source (see also the optical discovery spectrum by Jiang et al. 2008). Given the intrinsic weakness of the MgII emission, we do not include this QSO in the following analysis.

2.1.1. Data reduction

The ESO ISAAC pipeline produces wavelength calibrated co-added 2-D spectra from the individual frames that were acquired during each OB. Subsequent reduction was carried out within IRAF. One-dimensional spectra were extracted using the `apall` task. The tracing of the 1-D spectra was performed first on the bright stars in the slit. The resulting tracing functions were then used for the extraction of the QSO spectra. Individual 1D spectra were corrected for the telluric absorptions using the `telluric` task. Usually the telluric correction is performed by dividing the observed spectrum by the one of a telluric standard star observed shortly after the science target. This ratio is subsequently multiplied by the model atmosphere corresponding to the spectral type of the telluric standard and scaled to its observed K magnitude, in order to recover the correct slope of the QSO

spectrum. This operation allows us also to flux-calibrate the QSO spectrum. Instead of using the observed telluric standard stars, we employed the ESO sky absorption spectrum measured on the Paranal site at a nominal airmass of 1. This choice was driven by two reasons: i) the spectral regions in the QSO spectrum where telluric absorptions are most severe are characterized by a very low signal-to-noise, i.e. insufficient to properly correct for the actual detailed shape of the night sky features; ii) the observed telluric standard stars were often characterized by a spectral and luminosity class for which accurate model atmosphere could not be computed; the derived QSO continuum slope would have hence been distorted by the stellar spectral shape. We thus decided to focus on the spectral regions with higher signal, where an accurate correction was possible: we assumed the template sky absorption spectrum, scaled to the airmass of our QSO spectra and ignored the stability of the sky transparency. This way, we could preserve the intrinsic shape of the QSO continua. The `telluric` task corrects for the difference in airmass between the science and calibration spectra via the Beer-Lambert-Bouguer law. The telluric absorptions are in any case well removed from the spectra of bright QSOs, while significant residuals are left in the spectra of faint QSOs at lower S/N. The relative flux calibration was obtained with the `sensfunction`, `standard` and `calib` tasks. The instrument sensitivity function was obtained from the observed telluric stars of luminosity class V (giants) and spectral class B. For these stars it is possible to compute reliable model atmospheres since effective temperature and surface gravity are well estimated. The model atmospheres were computed by interpolating the NIR spectral energy distributions available from Pickles (1998) in temperature and surface-gravity in order to match the observed spectral type and magnitudes. After the relative flux calibration, the individual 1D QSO spectra were averaged to form a single spectrum. The absolute flux calibration was performed scaling the observed spectra to match the QSOs K-band magnitudes. Since the K-band magnitude was not measured for the QSOs in Tab. 1, we derived it from the SDSS QSO template scaled to the observed J and H-band magnitude. The whole reduction procedure was extensively tested on some of the observed telluric standard stars used as reference targets. The recovered spectra match the theoretical model atmospheres typically within 10%, even in the spectral regions more affected by telluric absorptions. The reduced spectra are shown in Fig. 3.4.

2.2. Literature Data

The QSOs taken from the literature are summarized in Tab. 2. We have collected a total of 22 spectra (19 different sources) which cover all the features of interest at sufficiently high S/N to perform the spectral decomposition (see Sec. 4.2 and Sec. 4.6). The literature sample is composed of 10 sources with $z < 5.70$ and 9 sources with $5.70 < z < 6.43$. The 10 QSOs with $z < 5.70$ are selected amongst the 13 sources published by Iwamuro et al. (2002). These QSOs have redshifts $4.4 < z < 5.3$ and were observed in the J and H bands with an OH-airglow suppressor spectrograph (OH-S), mounted on the Subaru Telescope. The spectral resolution ($\lambda/\Delta\lambda$) is equal to 210 (J band) and 420 (H band).

TABLE 1

SUMMARY OF THE NEWLY OBSERVED SOURCES. (1) QSO NAME; (2), (3) QSO RIGHT ASCENSION AND DECLINATION IN J2000.0 (FROM DISCOVERY PAPERS, COL [8]); (4) OPTICAL REDSHIFT (FROM DISCOVERY PAPERS); (5) z_{AB}^* (FROM DISCOVERY PAPERS); (6) K BAND NOMINAL MAGNITUDE, OBTAINED FROM THE REDSHIFTED SDSS QSO TEMPLATE SCALED TO MATCH THE OBSERVED J AND H-BAND MAGNITUDES (DISCOVERY PAPERS); (7) TOTAL ON SOURCE EXPOSURE TIME; (8) DISCOVERY PAPER: DRIP, DE ROSA ET AL. (IN PREP); J08, JIANG ET AL. (2008).

QSO name (1)	RA (2)	DEC (3)	z (4)	z_{AB}^* (5)	K (6)	t_{exp} (7)	Reference (8)
SDSS J0353 + 0104	03 53 49.72	+01 04 04.4	6.05	20.5	17.81	4.60 h	J08
SDSS J2054 - 0005	20 54 06.49	-00 05 41.8	6.06	20.7	17.87	5.92 h	J08
SDSS J0842 + 1218	08 42 29	+12 18 50.5	6.08	19.6	17.67	4.60 h	DRip

We also selected 2 of the 4 SDSS QSOs at $z \sim 6$ presented by Iwamuro et al. (2004): H and K observations were carried out with the Cooled Infrared Spectrograph and Camera (CISCO) mounted on the Subaru telescope, with a spectral resolution of 210 and 330 respectively. We used the K-band spectrum of the $z = 6.43$ QSO J1148+5251 published by Barth et al. (2003). Data were obtained with the NIRSPEC spectrograph on KeckII (spectral resolution of 1500). We selected 4 of the 5 sources presented by Kurk et al. (2007) at redshifts $z > 5.8$. The K-band observations were carried out with VLT-ISAAC with a spectral resolution of 450. We also included the K-band spectrum of J0303-0019 presented by Kurk et al. (2009). This faint $z \sim 6$ QSO was selected in SDSS Stripe 82 and its spectrum was taken with VLT-ISAAC. Finally, we added 4 SDSS QSOs at $z > 5.8$ published by Jiang et al. (2007), who observed them with GNIRS on Gemini South with a spectral resolution of 800.

3. DATA ANALYSIS

We focus on the spectral region with restframe wavelengths $2000 \text{ \AA} < \lambda_{rest} < 3500 \text{ \AA}$. This region is characterized by the presence of the Mg II emission line, the underlying non-stellar continuum, the Balmer pseudo continuum and the Fe II emission line forest. The last three emission features, that are overlapped in the spectral range of interest, are described in the following sections.

3.1. Power-law

The dominant component of a QSO spectrum is the non-stellar continuum, modeled as a power-law:

$$F_\lambda = F_0 \left(\frac{\lambda}{2500 \text{ \AA}} \right)^\alpha \quad (1)$$

Typically, in our data, the determination of the slope coefficient α depends on the adopted fitting procedure and on the observed spectral range. In case of a wide wavelength coverage it is possible to choose fitting windows free of contributions by other emission components. For spectra with restricted wavelength coverage, the power-law continuum has to be fitted simultaneously with the other components, resulting in a local estimate of the slope that might not be fully representative of the overall continuum shape of the QSO. Decarli et al. (2010) analyzed a sample of 96 QSOs at $z < 3$ by fitting the power-law continuum in 8 different windows free of strong features, and obtained a mean value for the slope of -1.3 with a $1-\sigma$ dispersion of 1.6. Shen et al. (2010)

estimated the local slope for a sample of $\sim 100,000$ SDSS QSOs at $z < 4.95$, fitting the the power-law plus an iron template to the wavelength range around four broad emission lines (H α , H β , Mg II and C IV). In particular, from the analysis of the wavelength range adjacent the Mg II emission line, they obtained a mean value for the local slope of -1.3 with a $1-\sigma$ dispersion of 0.8. From our spectral decomposition we find consistent values (see Sec. 3.4).

3.2. Balmer pseudo-continuum

We model the Balmer pseudo-continuum following Dietrich et al. (2003). We assume partially optically thick gas clouds with uniform temperature $T_e = 15000 \text{ K}$. For wavelengths below the Balmer edge ($\lambda_{BE} = 3646 \text{ \AA}$), the Balmer spectrum can be parametrized as:

$$F_\lambda = F_{norm} B_\lambda(T_e) (1 - e^{-\tau_{BE} (\frac{\lambda}{\lambda_{BE}})^3}), \quad \lambda < \lambda_{BE} \quad (2)$$

where $B_\lambda(T_e)$ is the Planck function at the electron temperature T_e , τ_{BE} is the optical depth at the Balmer edge (we assume $\tau_{BE} = 1$ following Kurk et al. 2007), and F_{norm} is the normalized flux density at the Balmer edge (Grandi 1982). The normalization should be determined at $\lambda_{rest} \simeq 3675 \text{ \AA}$, where no Fe II emission is present. Since this wavelength is either not covered or has a very low S/N in our sample, we fix the normalization to a fraction of the continuum strength extrapolated at 3675 \AA : $F_{norm} = f_B \cdot F_{power-law}(3675 \text{ \AA})$. To define the relative strength of the two components and monitor the effects on the Fe II estimate, we have run various tests with $f_B = 0.1, 0.3, 0.5, 0.8, 1$. Since differences in the Fe II estimates resulting from this test were less than measured errors (with f_B only partially affecting the power-law normalization), we have fixed $f_B = 0.3$ based on the results by Dietrich et al. (2003).

3.3. Fe II template

The Fe II ion emits a forest of lines, many of which are blended. We fit the Fe II forest using a modified version of the emission line template by Vestergaard & Wilkes (2001). This template is based on the high resolution spectrum of the narrow line Seyfert 1 galaxy PG0050+124 ($z=0.061$), observed with the Hubble Space Telescope. Vestergaard & Wilkes obtained the emission line template by first fitting and subtracting the power-law continuum and all the absorption/emission features from all the elements but Fe. Afterward an Fe III model was subtracted from the residual to obtain a pure Fe II

TABLE 2
LITERATURE SAMPLE SORTED BY REDSHIFT. (1) QSO NAME; (2), (3) QSO RIGHT ASCENSION AND DECLINATION IN J2000.0; (4) OPTICAL REDSHIFT FROM DISCOVERY PAPER; (5) NIR SPECTRUM REFERENCE PAPER FOR THE NIR SPECTRA: A IWAMURO ET AL. (2002), B IWAMURO ET AL. (2004), C BARTH ET AL. (2003), D KURK ET AL. (2007), E KURK ET AL. (2009), F JIANG ET AL. (2007).

QSO name (1)	RA (2)	DEC (3)	z (4)	Reference for NIR spectra (5)
BR 1033 – 0327	10 33 51.47	–03 27 45.5	4.51	A
BR 0019 – 1522	00 19 35.90	–15 22 16.0	4.53	A
BR 2237 – 0607	22 37 17.44	–06 07 59.7	4.56	A
SDSS J0310 – 0014	03 10 36.97	–00 14 57.0	4.63	A
SDSS J1021 – 0309	10 21 19.16	–03 09 37.2	4.70	A
SDSS J0210 – 0018	02 10 43.17	–00 18 18.4	4.77	A
SDSS J0211 – 0009	02 11 02.72	–00 09 10.3	4.90	A
PC 1247 + 3406	12 47 17.79	+34 06 12.7	4.90	A
SDSS J0338 + 0021	03 38 29.31	+00 21 56.3	5.00	A
SDSS J1204 – 0021	12 04 41.73	–00 21 49.6	5.03	A
SDSS J0005 – 0006	00 05 52.30	–00 06 56.0	5.85	D
SDSS J1411 + 1217	14 11 11.30	+12 17 37.0	5.93	D, F
SDSS J1306 + 0356	13 06 08.20	+03 56 26.0	5.99	D, F
SDSS J1630 + 4012	16 30 33.90	+40 12 10.0	6.05	B
SDSS J0303 – 0019	03 03 31.40	–00 19 12.9	6.07	E
SDSS J1623 + 3112	16 23 31.80	+31 12 01.0	6.22	F
SDSS J1048 + 4637	10 48 45.05	+46 37 18.3	6.23	B
SDSS J1030 + 0524	10 30 27.10	+05 24 55.0	6.28	D, F
SDSS J1148 + 5251	11 48 16.64	+52 51 50.3	6.43	C

template. As Kurk et al. (2007) pointed out, no Fe II emission is left in the 2770–2820 Å range, due to the Mg II line subtraction. We modified the template following Kurk et al. (2007) by adding a constant flux density between 2770 and 2820 Å equal to the 20% of the mean flux density of the template between 2930 and 2970 Å. The justification for this operation comes from the theoretical Fe II emission line strength by Sigut & Pradhan (2003). Since the Fe II and the Mg II are not distributed in the same way within the BLR, we decided not to fix the Doppler broadening of the Fe II template to the one measured for the Mg II emission line. We have instead run many tests broadening the Fe II template by convolving it with Gaussian profiles with constant FWHM = 7.5, 15, 22.5 Å, corresponding to FWHM ~ 930, 1860, 2800 km/s at 2400 Å respectively. A Gaussian broadening with σ constant in wavelength leads to slightly different velocities over the fitting range, but we have found no significant differences in the measured Fe II normalization in function of the three broadening. Given the typical S/N of our spectra the Fe II normalization is in fact mainly determined by the fit of the template broad bumps rather than individual Fe II features. We finally chose to fix FWHM = 15 Å for the Fe II template.

3.4. Fitting procedure

All the spectra have been shifted to the rest-frame system of reference using optical redshifts. Even if the optical redshifts are slightly different from the NIR ones, this will not affect our results since the Mg II peak wavelength is a free parameter in our fitting procedure. Moreover, the Fe II template is constituted by blended multiplets (broadened by the convolution with Gaussian profiles with FWHM = 15 Å), for which the definition of peak wavelength is not straightforward. We tested a posteriori the difference between the optical redshifts (see Tab. 1 and Tab. 2) and the ones measured from the Mg II peak

wavelength (see Tab. 4). The average difference is equal to $\Delta z = 0.02$ with a maximum of $\Delta z = 0.08$ for J1411+1217 (Jiang et al. 2007, online Appendix Fig. A.12) : in this case the Mg II line profile is severely affected by the atmospheric absorptions. Our spectra have different wavelength coverage because of the different redshifts of the sources and of the various instruments used to collect the data. Similarly the sky contamination varies across the sample with redshift. For these reasons it is impossible to define fixed fitting windows for the entire sample. We focus on the rest-frame region within 2000 and 3500 Å, choosing the fitting windows in a way as homogeneous as possible, as a function of the spectral coverage and of the sky contamination. The fit is performed in two steps. A first set of spectral components is given by the sum of the power-law continuum, the Balmer pseudo-continuum and the Fe II template. The free parameters are the power-law slope (α) and its normalization ($\beta = \log(F_0)$) and the Fe II template normalization (γ). Since the three components are overlapped in this wavelength range, the fit is performed with a χ^2 minimization on a suitable grid in the parameter space. In this way, we minimize the possibility that our solution represents only a local minimum of the χ^2 domain. The errors on the Fe II normalization are computed by marginalizing the probability distributions in 3-D parameter space, selecting all the cases for which $\chi^2 - \chi^2_{min} < 1$ (1σ confidence level). To ensure a reliable estimate of these errors we need enough triplets satisfying the χ^2 condition. After many tests we decided to sample the parameter space with 16 million points: 100 (α) \times 100 (β) \times 1600 (γ). This way, for each fit, we sample the γ parameter space with an average bin of 0.001×10^{-17} erg s $^{-1}$ cm $^{-2}$ and we obtain ~ 100 triplets satisfying the χ^2 , with a minimum of 15 (for the QSO BR 1033 – 0327). This condition is not satisfied for J0303 – 0019 (Kurk et al. 2009, online Appendix Fig. A.17): in this case the Fe II major features are severely affected by the telluric absorptions, resulting in

a weaker constraint on the Fe II template normalization which is in any case consistent with 0 (see Tab. 3). In Fig. 3.4 we show two examples of the 3D χ^2 -cube projections and of the relative probability distribution for the Fe II template normalization (similar plots for all sources discussed here are shown in the online Appendix). The χ^2 -maps are overall regular (non-patchy), implying the absence of secondary local minima. The degeneracy between power-law slope and intercept is evident from the bottom-right plots in the two panels.

The fitted components are then subtracted and we proceed to fit the Mg II emission line. The Mg II line fit is performed with a least-squares procedure. Since the Mg II doublet is not resolved in the majority of our spectra, we model the emission line as a simple Gaussian (three free parameters: central wavelength, width and normalization). If there was a significant narrow second component that we do not resolve, this would lead to a slight underestimate of the black-hole mass.

Examples of the spectral decomposition are shown in Fig. 3.4. The results of the fit and relative χ^2 maps for the literature sample are shown in the online Appendix. The fitted parameters are listed in Tab. 3. Even if we do not overcome the degeneracy between the power-law slope and intercept, we can compare the distribution of our local slope estimates with those in the literature. We obtain a mean value $\alpha = -1.5 \pm 1.2$ which is in agreement within the uncertainties with both the local slope estimate by Shen et al. (2008) and with the global one by Decarli et al. (2010).

4. RESULTS

4.1. Black hole mass estimate

We estimate the M_{BH} using scaling relations, calibrated on local AGNs, that are based on broad emission line widths and continuum luminosities. Under the assumption that the dynamics of the broad line region is dominated by the gravity of the central BH, the virial theorem states:

$$M_{BH} = G^{-1} R_{BLR} v_{BLR}^2 \quad (3)$$

where M_{BH} is the black hole mass, R_{BLR} is the characteristic radius of the BLR and v_{BLR} is the orbital velocity of the clouds emitting at R_{BLR} . The cloud velocity can be obtained from the width of the broad emission lines: $v_{BLR} = f \cdot FWHM$, where f is a geometrical factor that accounts for the de-projection of v_{BLR} from the line of sight (see McGill et al. 2008; Decarli et al. 2008), and FWHM is the full width at half maximum of the line profile. Even if the BLR size cannot be directly measured by single epoch spectra, it can still be evaluated since it is strongly correlated with the continuum luminosity of the AGN (e.g. Kaspi et al. 2000). It is then possible to estimate M_{BH} for high-redshift QSOs using a single spectrum covering the blended Mg II line doublet ($\lambda = 2795, 2803 \text{ \AA}$) and the redward continuum ($\lambda = 3000 \text{ \AA}$). In particular for R_{BLR} we use the relation provided by McLure & Jarvis (2002):

$$\frac{R_{BLR}(\text{Mg II})}{10 \text{ light - days}} = (2.52 \pm 0.03) \left[\frac{\lambda L_{\lambda}(3000 \text{ \AA})}{10^{44} \text{ erg s}^{-1}} \right]^{0.47} \quad (4)$$

and for the geometrical factor the value provided by Decarli et al. (2008): $f(\text{Mg II}) = 1.6$, obtained assuming that the Mg II and H β -emitting regions have a similar geometry. All these relations are based on low redshift objects ($z < 0.3$), and the underlying assumption here is that they are still valid at high-redshift. Using relation (4) McLure & Jarvis (2002) reproduced M_{BH} obtained with the full reverberation mapping method with an accuracy of 0.4 dex. This intrinsic scatter of the estimator dominates the measurement uncertainties. To compare our results with the ones published in previous works on $z \sim 6$ sources (Barth et al. 2003; Jiang et al. 2007; Kurk et al. 2007, 2009), we also estimate M_{BH} using the relation obtained by McLure & Dunlop (2004):

$$\frac{M_{BH}}{M_{\odot}} = 3.2 \left[\frac{\lambda L_{\lambda}(3000 \text{ \AA})}{10^{37} \text{ W}} \right]^{0.62} \left[\frac{FWHM(\text{Mg II})}{\text{km s}^{-1}} \right]^2 \quad (5)$$

from a sample of 17 low redshift AGNs ($z < 0.7$), with luminosities comparable to those of high- z QSOs ($\lambda L_{\lambda} > 10^{44} \text{ erg s}^{-1}$).

From the estimated M_{BH} we compute the QSO Eddington ratios defined as the ratio between the measured bolometric luminosity L_{bol} and the theoretical Eddington luminosity L_{Edd} , as computed from the M_{BH} . We obtain the observed monochromatic luminosity $\lambda L_{\lambda}(3000 \text{ \AA})$ from the continuum component of the fit $f_{\lambda}(3000 \text{ \AA})$ and from the luminosity distance D_L as:

$$\lambda L_{\lambda}(3000 \text{ \AA}) = \lambda F_{\lambda}(3000 \text{ \AA}) 4\pi D_L^2 \quad (6)$$

Since $L(3000 \text{ \AA})$ is only a fraction of the total electromagnetic luminosity coming from the QSO, we apply the bolometric correction by Shen et al. (2008) to obtain L_{bol} :

$$L_{bol} = 5.15 \lambda L_{\lambda}(3000 \text{ \AA}) \quad (7)$$

The Eddington luminosity is defined as the maximum luminosity attainable, at which the radiation pressure acting on the gas counterbalances the gravitational attraction of the BH:

$$L_{Edd} = 1.3 \cdot 10^{38} \left(\frac{M_{BH}}{M_{\odot}} \right) \text{ erg s}^{-1} \quad (8)$$

The obtained M_{BH} and the relative QSO Eddington ratios are listed in Tab. 4. The two relations, Eq. 4 and Eq. 5, lead to a difference in the mass estimates of a factor ~ 1.7 . The results obtained for the sample of published sources via Eq. 5 are in good agreement with previous estimates, indicating that different fitting procedures imply variations smaller than the errors due to the intrinsic scatter of the estimator. The average difference between the BH masses estimated by us and the ones previously published is equal to 0.1 dex. Only in the case of the QSO SDSS J0005-0006 (Kurk et al. 2007, online Appendix Fig. A.11) this difference is higher (0.7 dex): in this case the Mg II line is severely affected by the atmospheric absorption and the line fit becomes significantly procedure-dependent.

4.2. Dependence on the S/N and on the systematics in the observations

In Fig. 4.2 we show the M_{BH} obtained via Eq. 4 as a function of the S/N per \AA of the Mg II peak. The noise

TABLE 3

FITTED SPECTRAL PROPERTIES. THE SPECTRAL DECOMPOSITION HAS BEEN PERFORMED ON THE SPECIFIC FLUXES F_λ IN UNITS OF 10^{-17} ERG s^{-1} cm^{-2} \AA^{-1} . (1) QSO NAME. FOR SOURCES WITH MULTIPLE OBSERVATIONS: *, JIANG ET AL. (2007); +, KURK ET AL. (2007).; (2) POWER-LAW SLOPE; (3) FE II NORMALIZATION; (4) MG II CENTRAL WAVELENGTH [\AA]; (5) FWHM [$km s^{-1}$]; (6) MEASURED SPECIFIC FLUX OF THE CONTINUUM AT 3000 \AA , IN UNITS OF 10^{-17} ERG s^{-1} cm^{-2} \AA^{-1} . J0303 – 0019: THE FE II MAJOR FEATURES ARE SEVERELY AFFECTED BY THE TELLURIC ABSORPTIONS, RESULTING IN A WEAKER CONSTRAINT ON THE FE II TEMPLATE NORMALIZATION WHICH IS IN ANY CASE CONSISTENT WITH 0.

QSO name (1)	slope (2)	Fe II norm (3)	Mg II λ_{peak} (4)	Mg II FWHM (5)	F_λ (3000 \AA) (6)
BR 1033 – 0327	-2.4	0.84±0.02	2804.6±2.3	4248±120	8.20±1.59
BR 0019 – 1522	-2.3	1.01±0.03	2802.6±0.6	4317±120	7.78±1.50
BR 2237 – 0607	-1.3	1.57±0.36	2796.3±0.6	3811±163	19.98±0.12
SDSS J0310 – 0014	-1.5	0.24±0.05	2797.3±1.1	4087±260	2.83±0.05
SDSS J1021 – 0309	-1.7	0.26±0.09	2797.4±0.6	3100±162	2.76±0.09
SDSS J0210 – 0018	-2.7	0.11±0.06	2798.4±2.1	6543±803	3.42±0.05
SDSS J0211 – 0009	-2.4	0.38±0.05	2795.7±1.5	5975±468	1.44±0.28
PC 1247 + 3406	-2.2	0.30±0.10	2797.7±0.7	4094±197	3.86±0.08
SDSS J0338 + 0021	-1.8	0.51±0.05	2798.4±0.4	2969±128	3.20±0.05
SDSS J1204 – 0021	-2.3	0.83±0.03	2796.2±3.0	5753±208	4.36±0.04
SDSS J0005 – 0006	0.0	0.18±0.04	2796.2±0.1	1036±65	0.94±0.02
SDSS J1411 + 1217*	-1.7	0.20±0.07	2800.4±1.2	2208±317	2.39±0.06
SDSS J1411 + 1217+	1.2	0.36±0.04	2787.8±0.4	2824±168	3.03±0.05
SDSS J1306 + 0356*	-2.3	0.21±0.12	2809.5±0.5	3158±145	1.92±0.05
SDSS J1306 + 0356+	-2.5	0.13±0.13	2809.8±1.1	4134±351	1.97±0.04
SDSS J1630 + 4012	-0.7	0.03±0.03	2798.0±2.0	3366±533	1.46±0.30
SDSS J0303 – 0019	2.0	0.00±0.15	2802.28±0.4	2307±63	0.60±0.01
SDSS J1623 + 3112	0.0	0.31±0.02	2795.0±0.3	3587±118	1.81±0.05
SDSS J1048 + 4637	-1.7	0.56±0.03	2797.9±1.4	3366±532	4.22±0.04
SDSS J1030 + 0524*	-1.9	0.16±0.07	2807.2±0.6	3449±151	1.76±0.05
SDSS J1030 + 0524+	-1.3	0.17±0.08	2805.9±0.9	3704±231	1.88±0.03
SDSS J1148 + 5251	-2.1	0.91±0.01	2793.7±0.7	5352±289	4.22±0.08
SDSS J0353 + 0104	-2.2	0.43±0.06	2799.6±0.7	3682±281	2.16±0.10
SDSS J0842 + 1218	-0.9	0.38±0.06	2794.2±0.7	3931±257	2.38±0.12

was derived from regions of the spectra free of line emission. There is no evidence of any dependence of the M_{BH} estimates on the S/N of the Mg II line peak. For SDSS J1411 + 1217, SDSS J1306 + 0356 and SDSS J1030 + 0524 we are in the fortunate situation of having two independent observations by Jiang et al. (2007), with Gemini-GNIRS, and by Kurk et al. (2007), with VLT-ISAAC. We can thus use these to analyze the dependence of the M_{BH} estimates on the systematics in the observations. For these 3 sources Jiang et al. (2007) and Kurk et al. (2007) derived (using Eq. 5) 0.6, 1.1, $1.0 \times 10^9 M_\odot$ and 1.1, 2.4, $1.4 \times 10^9 M_\odot$, respectively. Using our fitting results and Eq. 5, we obtain 0.5, 0.9, $1.1 \times 10^9 M_\odot$ and 1.0, 1.7, $1.4 \times 10^9 M_\odot$ respectively, in good agreement with the published values. For those objects whose redshifts make their Mg II line fall on top of atmospheric absorption bands, the M_{BH} estimated from the two independent spectra can be significantly different (up to 0.3 dex in the case of SDSS J1306 + 0356): therefore we argue that the atmospheric contamination is a major contributor to systematics.

4.3. Comparison with SDSS QSO sample at $0.35 < z < 2.25$

To study the evolution of the BH population with cosmic time, we compare our sources with a sample of SDSS QSOs at lower redshift (SDSS Data Release 7, Shen et al. 2010). For objects with multiple observations we consider the weighted mean of the individual measurements. Since the M_{BH} estimates significantly depend on the

adopted estimator (see Peterson 2010; Shen et al. 2008), we select among the $\sim 100,000$ QSOs in the SDSS DR7 sample those with measurements of the Mg II FWHM and of $\lambda L_\lambda(3000\text{\AA})$: i.e., a subset of $\sim 47,000$ sources with $0.35 < z < 2.25$. We also consider a sample of nine $z \sim 6$ QSOs at lower luminosities ($M_{1450} < -24$) from Willott et al. (2010a), with published measurements of the Mg II FWHM and of $\lambda L_\lambda(3000\text{\AA})$. We obtain L_{bol} using the bolometric correction by Shen et al. (2008) (see Eq. 7) and we compute M_{BH} using Eq. 4, in analogy with the analysis performed in our sample. In Fig. 4.3 we plot the estimated M_{BH} as a function of the bolometric luminosity for the three samples. The black solid lines indicate regions of the parameter space with constant Eddington ratios: $L_{bol}/L_{Edd} = 0.01, 0.1, 1.0$. The $0.35 < z < 2.25$ and our high- z QSO populations occupy different regions of the parameter space: the $0.35 < z < 2.25$ redshift population shows an average $\langle \log(L_{bol}/L_{Edd}) \rangle \sim -1.2$ dex ($L_{bol}/L_{Edd} \sim 0.06$) with a dispersion of 0.3 dex, while the typical ratio for the high- z QSOs is $\langle \log(L_{bol}/L_{Edd}) \rangle \sim -0.3$ dex ($L_{bol}/L_{Edd} \sim 0.5$) with a dispersion of 0.3 dex. The lower luminosity $z \sim 6$ sample (Willott et al. 2010a) is characterized by lower M_{BH} but comparable Eddington ratios than the most luminous SDSS QSOs at the same redshift. We therefore conclude that the average Eddington ratio for the $z \sim 6$ QSO sample studied to date is significantly higher than the typical SDSS QSOs at $0.35 < z < 2.25$.

We have to specify that Shen et al. (2010) fit the spectra considering the power-law non-stellar contin-

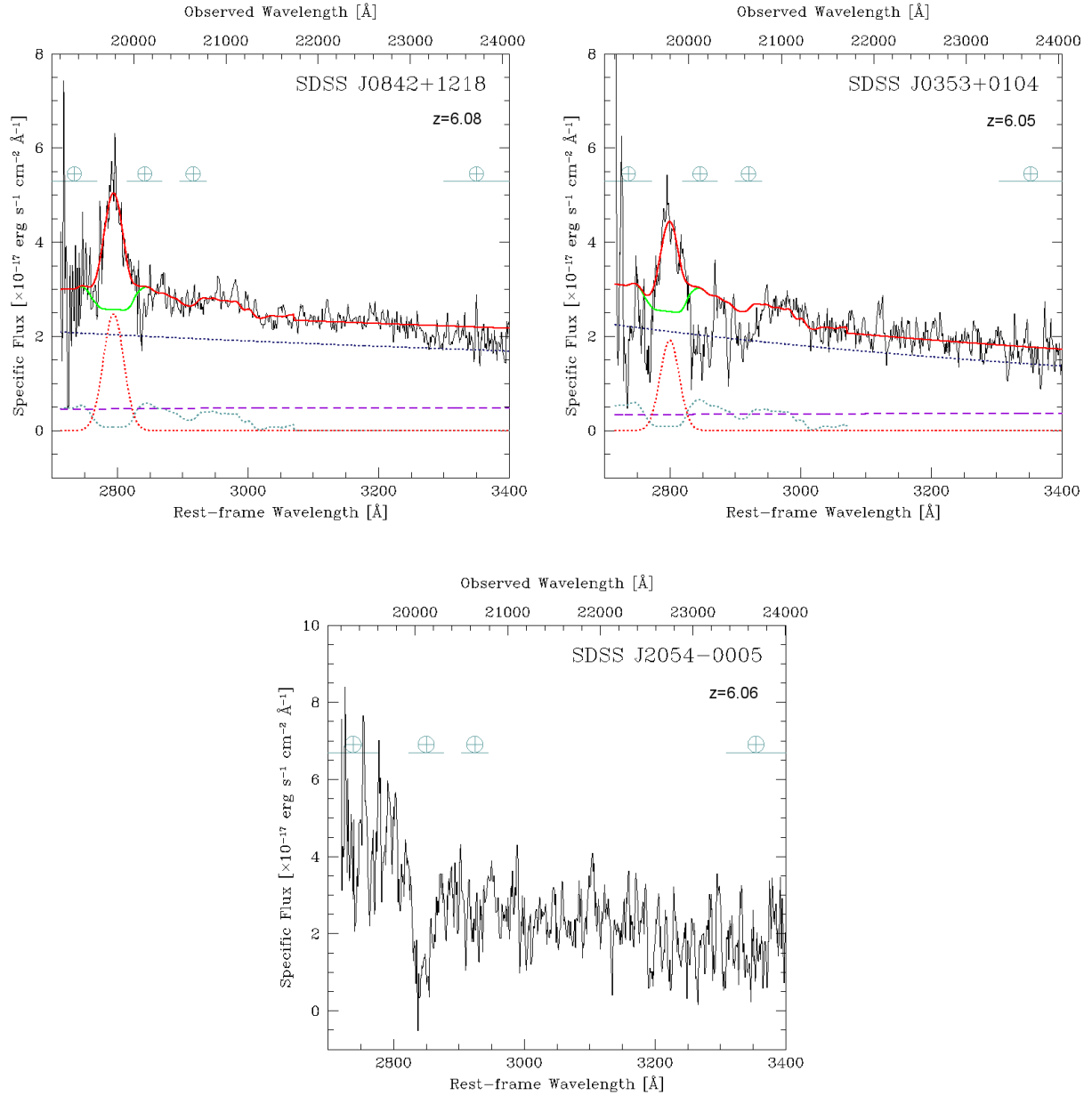


FIG. 1.— Reduced spectra of the QSOs SDSS J0842+1218 (upper-left panel), SDSS J0353+0104 (upper-right panel) and SDSS J2054-0005 (lower panel). The observed spectra are shown in black continuous line. The modeled components are: power-law continuum (blue dotted line), Balmer pseudo continuum (purple dashed line), Fe II normalized template (light blue dotted line), Mg II emission line (red dotted line). The sum of the first set of components (power-law continuum + Balmer pseudo continuum + Fe II normalized template) is overlotted to the spectrum as a green solid line, while the sum of all the components is over plotted as a red solid line. The spectral decomposition was not performed for the weak line QSO SDSS J2054-0005. Telluric absorption bands are indicated over the spectra with the symbol \oplus : they are extracted from the ESO sky absorption spectrum measured on the Paranal site at a nominal airmass of 1.

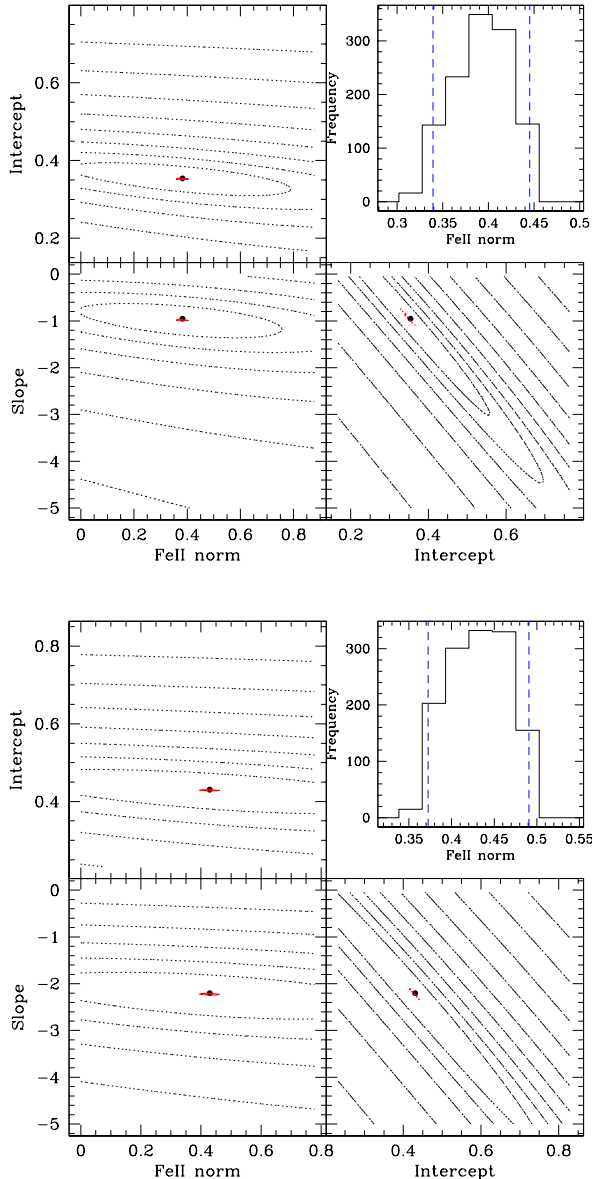


FIG. 2.— The Fe II normalization, obtained from the fit of the first set of components, depends on the power-law slope and its normalization (intercept). SDSS J0842+1218 (top panel) and SDSS J0353+0104 (bottom panel): χ^2 domain analysis for Fe II error computation. In each panel we show: a) two dimensional projections of the 3D χ^2 -surfaces (Fe II normalization vs Intercept, upper-left plot; Fe II normalization vs Slope, bottom-left plot; Intercept vs slope, bottom-right plot): contours represent iso- χ^2 levels spaced by a factor of 2 while the best fit case is marked with a dot; b) probability distribution for the Fe II template normalization (upper-right plot): the distribution has been obtained by marginalizing the 3-D probability distribution considering only the triplets for which $\chi^2 - \chi^2_{min} < 1$, the dashed vertical lines mark our estimate of the 1- σ confidence level.

uum, the Fe II line forest (modeled using the template by Vestergaard & Wilkes 2001), and both the narrow (simple Gaussian) and broad (simple/double Gaussian) components of the Mg II doublet. Since in our sample we are not subtracting the narrow component of the Mg II doublet (not resolved), the mass estimates of the high-redshift QSOs may be systematically biased towards slightly lower values with respect to the ones in the

$0.35 < z < 2.25$ redshift sample. Nevertheless, we note that our fitting procedure yields results consistent with the ones published by Jiang et al. (2007) who, except for the cases in which the line profile is severely affected by the atmospheric absorption, fits the Mg II emission line with a double Gaussian instead of a single one. Therefore, we conclude that the M_{BH} estimates do not strongly depend on the adopted fitting procedure.

4.4. Comparison with luminosity matched SDSS QSO sample

In order to perform a statistically robust comparison we now extract only objects with the same (high) bolometric luminosity: $10^{47} < L_{bol} [erg s^{-1}] < 3 \times 10^{47}$ from our sample and from the SDSS comparison sample at $0.35 < z < 2.25$. In Fig. 4.4 we plot the M_{BH} and the Eddington ratio as a function of redshift. The average M_{BH} at high- z is systematically lower than the typical M_{BH} of the $0.35 < z < 2.25$ population at similar luminosities, while the Eddington ratio is higher. Comparing the Eddington ratio distribution of the two luminosity matched samples (Fig. 4.4, $10^{47} < L_{bol} [erg s^{-1}] < 3 \times 10^{47}$) we obtain that for the $0.35 < z < 2.25$ population $\langle \log(L_{bol}/L_{Edd}) \rangle \sim -0.80$ dex ($L_{bol}/L_{Edd} \sim 0.16$) with a dispersion of 0.24 dex, while for the high- z one $\langle \log(L_{bol}/L_{Edd}) \rangle \sim -0.37$ dex ($L_{bol}/L_{Edd} \sim 0.43$) with a dispersion of 0.20 dex. If we perform a Kolmogorov-Smirnov test on the two distributions we obtain that the probability that they come from the same parent distribution is 7×10^{-9} , i.e. negligible. This implies that the high-redshift QSOs in this luminosity bin are building up their mass more rapidly than the ones at $z \sim 2$ (in agreement with what has been found for subsamples in previous studies, e.g. Kurk et al. 2009; Willott et al. 2010).

Another bias that could possibly affect our comparison between the high- z Eddington ratio distribution and the lower- z one is the intrinsic luminosity of the QSO broad lines. For instance the equivalent width of high ionization lines in AGN is known to anti-correlate with the continuum luminosity (Baldwin 1977; Baskin & Laor 2004;

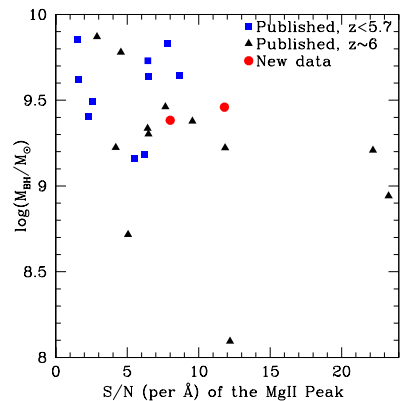


FIG. 3.— M_{BH} estimates as a function of the S/N per \AA at the Mg II peak. Blue squares: literature sample, at $z < 5.7$ (Iwamuro et al. 2002); black triangles: literature sample, $z \sim 6$ (Barth et al. 2003; Iwamuro et al. 2004; Jiang et al. 2007; Kurk et al. 2007, 2009); red circles: this study. Our M_{BH} estimates do not depend on the S/N of the QSO spectra.

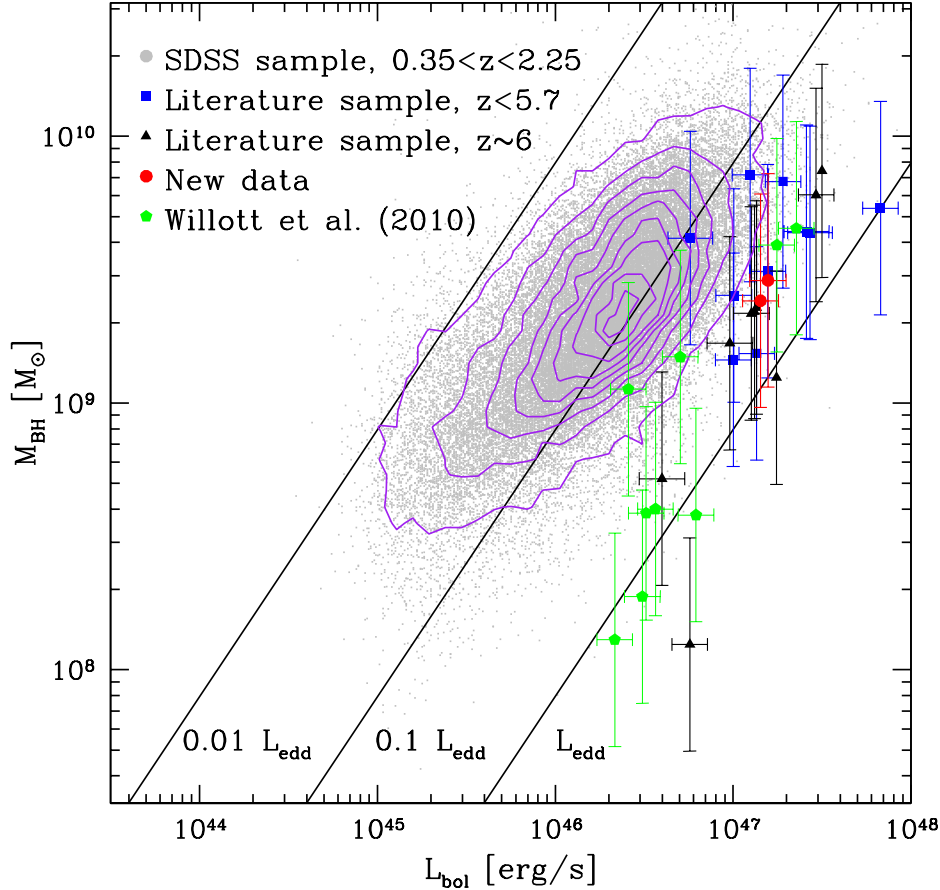


FIG. 4.— M_{BH} as a function of the bolometric luminosity: comparison between the present dataset and the SDSS QSOs sample at $0.35 < z < 2.25$. Blue squares: literature sample, $z < 5.7$ (Iwamuro et al. 2002); black triangles: literature sample, $z \sim 6$ (Barth et al. 2003; Iwamuro et al. 2004; Jiang et al. 2007; Kurk et al. 2007, 2009); red diamonds: new observations; green pentagons: CFHQS QSO sample (Willott et al. 2010); grey dots: SDSS QSOs sample $0.35 < z < 2.25$ (DR7, Shen et al. 2010); purple lines: isodensity contours. The black solid lines indicate regions of the parameter space with constant Eddington ratios: $L_{\text{bol}}/L_{\text{Edd}} = 0.01, 0.1, 1.0$. The $0.35 < z < 2.25$ and our high- z QSO populations occupy different regions of the parameter space: the $0.35 < z < 2.25$ redshift population shows $\langle \log(L_{\text{bol}}/L_{\text{Edd}}) \rangle \sim -1.2$ dex with a dispersion of 0.3 dex, while the typical ratio for the high- z QSOs is $\langle \log(L_{\text{bol}}/L_{\text{Edd}}) \rangle \sim -0.3$ dex with a dispersion of 0.3 dex.

Shang et al. 2003; Xu et al. 2008). This effect is a function of the line ionization potential and not observed in low ionization lines (e.g. Mg II line, Espey & Andreadis 1999). High- z QSOs are usually selected in function of their photometric colors as drop-out objects. This criterion is to some extent insensitive to the line brightness. For the SDSS QSOs sample with $0.35 < z < 2.25$ the existence of a broad line feature is instead required in addition to the color selection, resulting into a bias against weak line QSOs. Decarli et al. (2011) found that for the DR7 SDSS QSO sample (Shen et al. 2010) the Mg II line luminosity positively correlates with the continuum luminosity. Selecting objects within a given Mg II line luminosity bin would then result in a continuum luminosity cut, like the one previously taken into account.

4.5. Impact on BH formation history

Accurate measurements of BH masses and relative Eddington ratios of $z \sim 6$ QSOs can be used to give constraints on the formation processes of super-massive BHs

(SMBHs) in the early universe. The three outstanding theories for SMBH seed formation differ both in the astrophysical processes considered and in the resulting masses of the seeds: (i) BHs seeds of few hundreds of M_{\odot} can be produced by the first generation of stars (Pop III stars), formed out of zero metallicity gas; (ii) BH seeds of $10^2 - 10^4 M_{\odot}$ can be obtained via stellar-dynamical processes amongst Pop II stars; (iii) BH seeds of $10^4 - 10^5 M_{\odot}$ can be produced via gas-dynamical processes (direct collapse of dense gas clouds) (see Volonteri 2010, for a review on the SMBH formation).

We here consider only the 20 QSOs at $z \sim 6$, since they provide tighter constraints on the SMBH formation: 11 sources from our sample ($z > 5.7$) and 9 QSOs by Willott et al. (2010a). The resulting sample includes all the faint $z \sim 6$ QSOs known to date with estimated M_{BH} from the Mg II line. For this $z \sim 6$ population we obtain $\langle \log(M_{\text{BH}}/M_{\odot}) \rangle \sim 9.06$ dex ($M_{\text{BH}} \sim 1.1 \times 10^9 M_{\odot}$) with a dispersion of 0.5 dex and $\langle \log(L_{\text{bol}}/L_{\text{Edd}}) \rangle \sim -0.23$ dex ($L_{\text{bol}}/L_{\text{Edd}} \sim 0.6$) with a dispersion of 0.29 dex. The time needed by a BH seed to grow at a constant rate from an initial mass M_0 to a final mass M_t is equal to

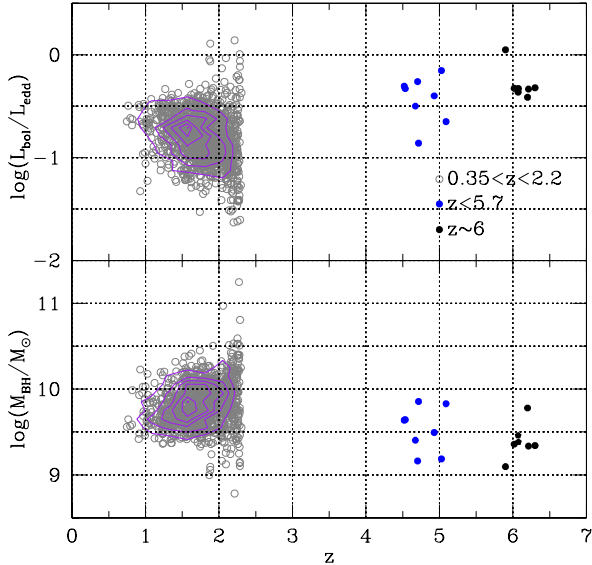


FIG. 5.— Eddington ratio (upper panel) and M_{BH} (lower panel) as a function of redshift for subsamples of QSOs with bolometric luminosities $10^{47} < L_{\text{bol}} [\text{erg s}^{-1}] < 3 \times 10^{47}$ extracted from the $0.35 < z < 2.25$ sample and from our high- z sample. Blue circles: $z < 5.7$ (Iwamuro et al. 2002); black circles: $z \sim 6$ (Barth et al. 2003; Iwamuro et al. 2004; Jiang et al. 2007; Kurk et al. 2007, 2009, this study); grey circles: SDSS QSOs sample $0.35 < z < 2.25$ (DR7, Shen et al. 2010); purple lines: isodensity contours. The average M_{BH} at high- z is lower than the typical M_{BH} of the $0.35 < z < 2.25$ population at similar luminosities, while the Eddington ratio is higher.

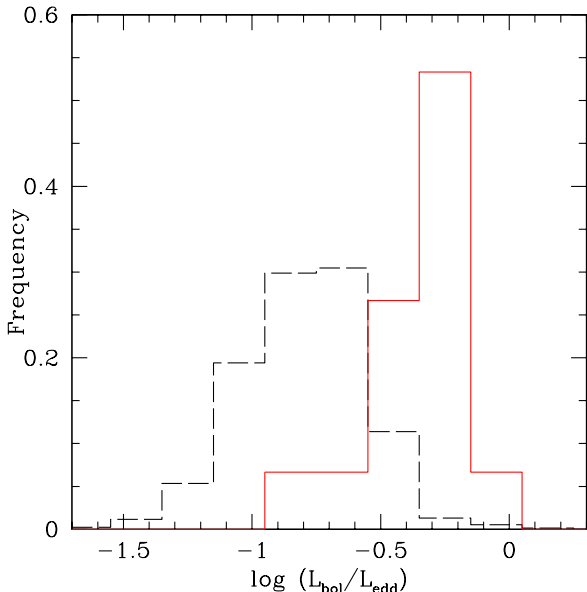


FIG. 6.— Eddington ratio distributions for sub samples of QSOs with bolometric luminosities $10^{47} < L_{\text{bol}} [\text{erg s}^{-1}] < 3 \times 10^{47}$ extracted from the $0.35 < z < 2.25$ sample and from our high- z sample: a) black dashed line: SDSS QSOs at $0.3 < z < 2.2$ (SDSS DR7, Shen et al. 2010); b) red solid line: our sample at $4.7 < z < 6.5$. The two distributions are intrinsically different: for the $0.35 < z < 2.25$ population $\langle \log(L_{\text{bol}}/L_{\text{Edd}}) \rangle \sim -0.80$ dex with a dispersion of 0.24 dex, while for the high- z one $\langle \log(L_{\text{bol}}/L_{\text{Edd}}) \rangle \sim -0.37$ dex with a dispersion of 0.20 dex. The Kolmogorov-Smirnov probability that the two distributions come from the same parent distribution is negligible.

(Volonteri & Rees 2005):

$$t = 0.45 \text{ Gyr} \times \left[\frac{\epsilon}{1-\epsilon} \right] \times \frac{L_{\text{edd}}}{L_{\text{bol}}} \times \ln \left(\frac{M_t}{M_0} \right) \quad (9)$$

where 0.45 Gyr is the Salpeter time, ϵ is the radiative efficiency ($\epsilon \sim 0.07$, Volonteri & Rees 2005), and $L_{\text{bol}}/L_{\text{edd}}$ is the Eddington ratio. A BH seed with mass $M_0 = 10^2, 10^5 M_{\odot}$ accreting constantly at the Eddington ratio characteristic of our population ($L_{\text{bol}}/L_{\text{edd}} \sim 0.6$), would then need a time $t \sim 0.91, 0.53$ Gyr, respectively, to obtain a final mass M_t equal to the mean M_{BH} of our sample.

If the characteristic Eddington ratio of the ~ 6 QSO population is well represented by our mean estimate, models with BH seed masses $\sim 10^2 M_{\odot}$ become problematic since the time needed for the seed to grow is comparable to the age of the universe at $z \sim 6$ (~ 0.9 Gyr). Moreover, since our QSOs are selected from flux-limited surveys the resulting distribution of the Eddington ratios should be biased towards higher values: BHs with low accretion rates may not pass the QSO selection magnitude limits. Kelly et al. (2010) and Willott et al. (2010a) have shown that the intrinsic Eddington ratio distribution for a volume limited QSO sample is indeed shifted towards lower values with respect to a luminosity selected population. Our estimate hence represents an upper limit of the characteristic Eddington ratio of the $z \sim 6$ QSO population: lower Eddington ratios, according to Eq. 9, would yield even longer time for the BH seeds to grow. In the future, with complete samples of QSOs at $z \sim 6$, it will be possible to give better constraints on the super massive BHs formation models.

4.6. Fe II/Mg II

An estimate of the Fe/Mg abundance ratio at $z \sim 6$ may serve as an indication of the onset of star formation in the highest- z QSOs (see Sec. 1). The proxy usually used to trace the Fe/Mg abundance ratio at high- z is the Fe II/Mg II line ratio. In the past, numerous NIR-spectroscopy studies have been carried out to analyze the Fe II/Mg II line ratio in high- z QSOs (e.g. Maiolino et al. 2001, 2003; Pentericci et al. 2002; Iwamuro et al. 2002, 2004; Barth et al. 2003; Dietrich et al. 2003; Freudling et al. 2003; Willott et al. 2003; Jiang et al. 2007; Kurk et al. 2007). The combined results revealed an increase in the scatter of the measured Fe II/Mg II line ratios as a function of redshift (see Kurk et al. 2007). A proposed explanation for the increased scatter is that some young objects have been observed such a short time after the initial starburst that the BLR has not been fully enriched with Fe yet.

We compute the Fe II flux by integrating the normalized Fe II template over the rest-frame wavelength range $2200 \text{ \AA} < \lambda_{\text{rest}} < 3090 \text{ \AA}$. The Mg II flux is computed by integrating the fitted single Gaussian over the range $\lambda_{\text{peak}} \pm 5\sigma$. The resulting Fe II/Mg II flux ratios and relative errors are listed in Tab. 4. In Fig. 4.6 we show the evolution of the Fe II/Mg II as a function of z (for objects with multiple observations we consider the weighted mean of the individual measurements). The reported scatter at $z \sim 6$ (Kurk et al. 2007) is now significantly reduced: our measurements of the line ratios span a range $0 < \text{Fe II/Mg II} < 6$, while previous results were dis-

TABLE 4
ESTIMATED M_{BH} , QSO EDDINGTON RATIOS AND $\text{Fe II}/\text{Mg II}$ LINE RATIOS. THE MASS ESTIMATES HAVE AN ACCURACY OF 0.4 DEX THAT DOMINATES THE MEASUREMENT UNCERTAINTIES. (1) QSO NAME. FOR SOURCES WITH MULTIPLE OBSERVATIONS: *, JIANG ET AL. (2007); +, KURK ET AL. (2007); (2) REDSHIFT ESTIMATE FROM Mg II LINE; (3) M_{BH} IN UNITS OF $10^9 M_{\odot}$ ESTIMATED USING EQ. 4; (4) M_{BH} IN UNITS OF $10^9 M_{\odot}$ ESTIMATED USING EQ. 5; (5) EDDINGTON ACCRETION RATIO DERIVED FROM M_{BH} COL. [2]; (6) EDDINGTON ACCRETION RATIO DERIVED FROM M_{BH} COL. [3]; (7) $\text{Fe II}/\text{Mg II}$ RATIO.

QSO name (1)	z (2)	M_{BH} [$10^9 M_{\odot}$]		$L_{\text{bol}}/L_{\text{edd}}$		$\text{Fe II}/\text{Mg II}$ (7)
		Eq. 4 (3)	Eq. 5 (4)	Eq. 4 (5)	Eq. 5 (6)	
BR 1033 – 0327	4.521±0.005	4.3	2.8	0.5	0.8	2.6±0.1
BR 0019 – 1522	4.534±0.001	4.4	2.8	0.5	0.7	2.7±0.1
BR 2237 – 0607	4.561±0.001	5.4	4.0	1.0	1.3	2.1±0.5
SDSS J0310 – 0014	4.672±0.002	2.5	1.4	0.3	0.6	2.7±0.6
SDSS J1021 – 0309	4.703±0.001	1.5	0.8	0.5	1.0	3.3±1.1
SDSS J0210 – 0018	4.715±0.004	7.2	4.1	0.1	0.2	1.5±0.9
SDSS J0211 – 0009	4.894±0.003	4.1	2.1	0.1	0.2	4.2±0.6
PC 1247 + 3406	4.929±0.001	3.1	1.9	0.4	0.7	2.1±0.7
SDSS J0338 + 0021	5.027±0.001	1.5	0.9	0.7	1.2	5.0±0.6
SDSS J1204 – 0021	5.090±0.007	6.8	4.1	0.2	0.4	3.3±0.1
SDSS J0005 – 0006	5.844±0.001	0.1	0.06	3.6	7.1	4.7±1.1
SDSS J1411 + 1217*	5.854±0.003	0.9	0.5	1.3	2.2	2.0±0.7
SDSS J1411 + 1217+	5.903±0.001	1.6	1.0	0.9	1.5	2.9±0.5
SDSS J1306 + 0356*	6.017±0.001	1.7	0.9	0.6	1.0	4.8±2.7
SDSS J1306 + 0356+	6.018±0.003	2.9	1.7	0.3	0.6	1.5 ^{+1.6} _{-1.5}
SDSS J1630 + 4012	6.058±0.005	1.7	0.9	0.5	0.8	0.5±0.5
SDSS J0303 – 0019	6.079±0.001	0.5	0.3	0.6	1.3	0.0±5.8
SDSS J1623 + 3112	6.211±0.001	2.2	1.2	0.5	0.8	4.3±3.3
SDSS J1048 + 4637	6.198±0.004	6.0	3.9	0.4	0.6	4.1±0.3
SDSS J1030 + 0524*	6.302±0.001	2.0	1.1	0.5	0.9	2.9±1.3
SDSS J1030 + 0524+	6.299±0.002	2.4	1.4	0.5	0.8	2.3±1.2
SDSS J1148 + 5251	6.407±0.002	7.4	4.9	0.3	0.5	4.6±0.2
SDSS J0353 + 0104	6.072±0.002	2.4	1.4	0.5	0.8	4.7±0.7
SDSS J0842 + 1218	6.069±0.002	2.9	1.7	0.4	0.7	3.1±0.5

tributed up to $\text{Fe II}/\text{Mg II} \sim 15$. The $\text{Fe II}/\text{Mg II}$ line measurements do not show any clear dependence on the estimated S/N per Å of the spectral continuum (see Fig. 4.6). On the other hand, our flux ratio estimates are well in agreement with previous results by Kurk et al. (2007) who performed an analysis similar to ours. We can conclude that this measurement is significantly dependent on the performed analysis, rather than on the S/N of the spectra. This result immediately implies that we do not need to invoke different chemical evolutionary stages of the BLR gas. We do not see evidence for evolution of the estimated $\text{Fe II}/\text{Mg II}$ line ratio as a function of cosmic age for $4 < z < 6.5$. Moreover, if we consider the SDSS QSO sample at $0.35 < z < 2.25$ (Shen et al. 2010, see Sec. 4.3), and we compute the $\text{Fe II}/\text{Mg II}$ line ratio starting from the published Fe II and Mg II flux measurements, we see no evolution of the line ratio also for $0.35 < z < 2.25$. However it is not possible to perform a direct comparison between the two samples, since these line ratio measurements are highly dependent on the adopted fitting procedure.

To constrain the onset of the star formation in these early QSOs, we would need to derive an estimate of the Fe/Mg abundance ratio from the measurements of the $\text{Fe II}/\text{Mg II}$ line ratio. Unfortunately, an accurate conversion cannot be performed since the detailed formation of the Fe II bump in QSO spectra has not been fully understood yet. Wills et al. (1985) discussed the suitability of the $\text{Fe II}/\text{Mg II}$ line ratio as a proxy of the Fe/Mg abundance ratio, as the regions in which the two ions are

produced and the radiative transfer of the two lines are both very different. Computing the Fe II and Mg II line strength for a gas with cosmic abundances and using a wide range of hydrogen densities and ionization parameters, they predicted typical $\text{Fe II}/\text{Mg II}$ line ratios between 1.5 and 4.0 (this is indicated in Fig. 4.6 as a grey-shaded area), and attributed higher $\text{Fe II}/\text{Mg II}$ values to an overabundance of Fe with respect to Mg. However these computations were based on a limited 70-level model of the Fe atom. Baldwin et al. (2004) used a 371-level Fe^+ model to reproduce the observed Fe II emission properties in AGNs considering a large set of models of broad emission line region clouds. From their results, all the observed Fe II features can be reproduced only if: (i) the BLR is characterized by the presence of significant microturbulence; (ii) the Fe II emitting gas has different properties (density and/or temperature) with respect to the gas emitting other broad lines. In any case the strength of the Fe II emission relative to the emission line of other ions (e.g the $\text{Fe II}/\text{Mg II}$ line ratio) depends as much on the Fe abundance as it does on other physical parameters of the BLR (e.g. turbulence velocity), making it difficult to convert the observed line ratios in abundance ratios. Nevertheless, the study of the $\text{Fe II}/\text{Mg II}$ line ratio as a function of look-back time can be used to give constraints on the BLR chemical enrichment history, under the assumption that physical conditions of the BLR that determine the Fe II emission are not evolving.

The observed lack of evolution in the measured $\text{Fe II}/\text{Mg II}$ line ratio can then be explained with an early

chemical enrichment of the QSO host. I.e. the QSOs in our sample must have undergone a major episode of Fe enrichment in a few hundreds Myr before the cosmic age at which they have been observed (~ 0.9 Gyr). Matteucci & Recchi (2003) showed that for a massive elliptical galaxy characterized by a very intense but short star-formation history, the typical timescale for the maximum SN Ia rate can be as short as 0.3 Gyr. This implies that if the Fe in high- z QSO hosts is mainly produced via SN Ia explosions, it would be possible to observe fully enriched BLR at $z \sim 6$. On the other hand, Venkatesan et al. (2004) pointed out that SNe Ia are not necessarily the main contributors to the Fe enrichment, and that stars with a present-day initial mass function are sufficient to produce the observed Fe II/Mg II line ratios at $z \sim 6$. Fe could also be generated by Pop III stars: these very metal poor stars with typical masses $M \gtrsim 100 M_{\odot}$ might be able to produce large amounts of Fe within a few Myr (Heger & Woosley 2002).

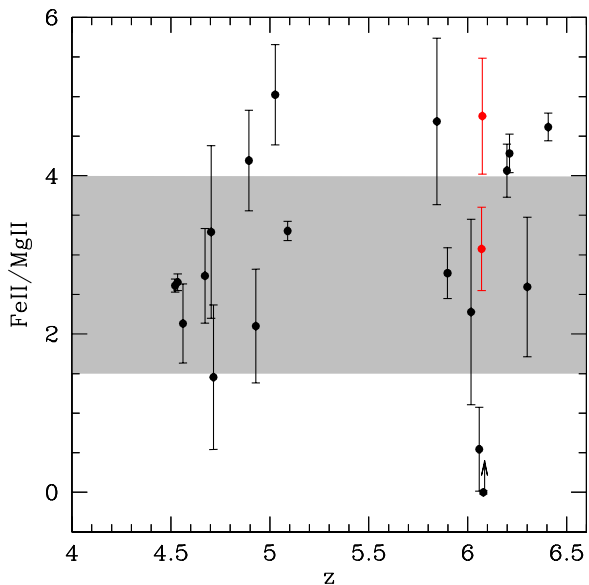


FIG. 7.— Evolution of the Fe II/Mg II line ratio for $z > 4$. Black points: literature sample, $z > 4.4$; red points: new targets. Grey-shaded area: expected Fe II/Mg II line ratio obtained by modeling the Fe II and Mg II line strength considering gas with cosmic abundance and a range of ionizing continua (Wills et al. 1985). The reported scatter at $z \sim 6$ (Kurk et al. 2007) is now significantly reduced: our measurements of the line ratios span a range $0 < \text{Fe II/Mg II} < 6$, while previous results were distributed up to $\text{Fe II/Mg II} \sim 15$. No redshift evolution of the Fe II/Mg II ratio is observed for $4 < z < 6.5$.

5. SUMMARY AND CONCLUSIONS

We presented NIR-spectroscopic observations of three $z \sim 6$ SDSS QSOs. Our NIR spectra cover the Mg II and Fe II emission features, which are powerful probes of M_{BH} and of the chemical enrichment of the BLR. The new data extend the existing SDSS sample towards the faint end of the QSO luminosity function. We have collected 22 literature spectra (19 different sources) of high-redshift ($z > 4$) QSOs covering the rest-frame wavelength range $2700 \text{ \AA} < \lambda < 3200 \text{ \AA}$. The final sample is composed of 22 sources: our three new sources

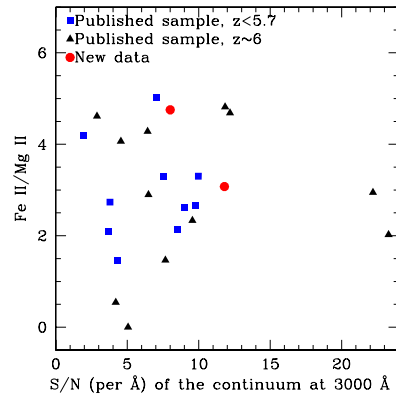


FIG. 8.— Fe II/Mg II line ratio estimates as a function of the S/N per \AA of spectral continuum at 3000 \AA . Blue squares: literature sample, at $z < 5.7$ (Iwamuro et al. 2002); black triangles: literature sample, $z \sim 6$ (Barth et al. 2003; Iwamuro et al. 2004; Jiang et al. 2007; Kurk et al. 2007, 2009); red circles: new observations. The Fe II/Mg II line measurements do not show a dependence on the S/N per \AA of the spectral continuum.

at $z \sim 6$, 10 spectra from the literature of QSOs with $4 < z < 5.7$ (Iwamuro et al. 2002) and 9 spectra of QSOs with $z \sim 6$ (Barth et al. 2003; Iwamuro et al. 2004; Jiang et al. 2007; Kurk et al. 2007, 2009). In order to see how the derivation of physical parameters depend on the fitting strategy employed, we performed a new consistent analysis of the sample and we gave an estimate of the M_{BH} , of the $L_{\text{bol}}/L_{\text{Edd}}$ and of the Fe II/Mg II line ratio.

Our results and conclusions can be summarized as follows:

1. We have estimated the M_{BH} from the Mg II emission line using empirical mass scaling relations. The QSOs in our sample host BHs with masses of $\sim 10^9 M_{\odot}$. Our results are in good agreement with previous estimates, indicating that different fitting procedures imply variations smaller than the errors due to the intrinsic scatter of the M_{BH} estimator.
2. High-redshift QSOs are accreting close to the Eddington luminosity: $\langle \log(L_{\text{bol}}/L_{\text{Edd}}) \rangle \sim -0.3$ dex ($L_{\text{bol}}/L_{\text{Edd}} \sim 0.5$) with a dispersion of 0.3 dex. The distribution of observed Eddington ratios is significantly different (average Eddington ratio ~ 8 times higher) from that of a comparison sample at $0.35 < z < 2.25$ (SDSS, DR7). This result is not biased by the luminosity selection of the high- z sample: the difference in the two Eddington ratio distributions persists even considering two luminosity matched subsamples ($z \sim 6$ average Eddington ratio ~ 3 higher than lower redshift one). The high- z sources are accreting faster than the ones at $0.35 < z < 2.25$.
3. We calculated fluxes for the Mg II and Fe II lines. The obtained values are not always in agreement with the published ones, indicating that these measurements are dependent on the performed analysis. The previously observed scatter in the Fe II/Mg II line ratio at $z \sim 6$ is significantly reduced in this work: the BLRs in the highest- z

QSOs studied to date all show comparable level of chemical enrichment.

4. No redshift evolution of the Fe II/Mg II ratio is observed for $4 < z < 6.5$. If we consider the Fe II/Mg II line ratio as a second order proxy for Fe/Mg, this indicates that the QSOs in our sample must have undergone a major episode of Fe enrichment in the few hundreds Myr preceding the cosmic time at which the sources are observed.
5. Our results do not show any significant dependence on the S/N of the spectra: the M_{BH} estimates do not correlate with the S/N per Å of the Mg II line and the Fe II/Mg II line ratios do not show any clear dependence on the S/N per Å of the spectral continuum.

Even though the currently faintest known QSOs are included in the study we presented here (Willott et al.

2010a; Kurk et al. 2009), we are still not probing the bulk of QSOs that should be present at that redshift. Future studies of QSOs that populate the faint end of the QSO luminosity function at $z \sim 6$ are needed to investigate whether or not the results found here are applicable to all $z \sim 6$ QSOs.

We are indebted to A. J. Barth, W. Freudling, F. Iwamuro, Y. Juárez and R. Maiolino who have generously provided their spectra for this analysis. GDR thanks Marianne Vestergaard, Mauricio Cisternas and Mario Gennaro for the useful discussion. GDR is supported by the Deutsche Forschungsgemeinschaft priority program 1177. XF and LJ acknowledge support by NSF grant AST-0806861 and Packard Fellowship for Science and Engineering. JK thanks the DFG support via German-Israeli Project Cooperation grant STE1869/1-1.GE625/15-1.

REFERENCES

- Baldwin, J. A., 1977, ApJ 214:679
 Baldwin, J. A., Ferland, G. J., Korista, K. T., Hamann, F., LaCluyzé, A., 2004, ApJ 615:610
 Barth, A. J., Martini, P., Nelson, C. H., Ho, L. C., 2003, ApJ 594L:95
 Baskin, A., Laor, A., 2004, MNRAS 350:L31
 Decarli, R., Dotti, M., Treves, A., 2011, MNRAS, 413:39
 Decarli, R., Falomo, R., Treves, A., Labita, M., Kotilainen, J. K., Scarpa, R., 2010, MNRAS 402:2453
 Decarli, R., Labita, M., Treves, A., Falomo, R., 2008, MNRAS 387:1237
 Dietrich, M., Hamann, F., Appenzeller, I., Vestergaard, M., 2003, ApJ 596:817
 Fan, X., et al., 2000, AJ 120:1167
 Fan, X., et al., 2001, AJ 122:2833
 Fan, X., et al., 2003, AJ 125:1649
 Fan, X., et al., 2004, AJ 128:515
 Fan, X., et al., 2006, AJ 131:1203
 Freudling, W., Corbin, M. R., Korista, K. T., 2003, ApJ 587L:67
 Espey, B. R., Andreadis, S., 1999, in ASP Conf. Ser. 162, Quasars and Cosmology, ed. G.J. Ferland & J. A. Baldwin (San Francisco: ASP), 351
 Grandi, S. A., 1982, ApJ 255:25
 Hamann, F., Ferland, G., 1992, ApJ 391L:53
 Hamann, F., Ferland, G., 1993, ApJ 418:11
 Hamann, F., Korista, K. T., Ferland, G. J., Warner, C., Baldwin, J., 2002, ApJ 564:592
 Heger, A., Woosley, S. E., 2002, ApJ 567:532
 Hopkins, P. F., Hernquist, L., Cox, T. J., Di Matteo, T., Martini, P., Robertson, B., Springel, V., 2005, ApJ 630:705
 Iwamuro, F., Kimura, M., Eto, S., Maihara, T., Motohara, K., Yoshii, Y., Doi, M., 2004, ApJ 614:69
 Iwamuro, F., Motohara, K., Maihara, T., Kimura, M., Yoshii, Y., Doi, M., 2002, ApJ 565:63
 Jiang, L., et al., 2008, AJ 135:1057
 Jiang, L., et al., 2009, AJ 138:305
 Jiang, L., Fan, X., Vestergaard, M., Kurk, J. D., Walter, F., Kelly, B. C., Strauss, M. A., 2007, AJ 134:1150
 Kaspi, S., Smith, P. S., Netzer, H., Maoz, D., Jannuzi, B. T., Giveon, U., 2000, ApJ 533:631
 Kauffmann, G., Haehnelt, M., 2000, MNRAS 311:576
 Kelly, B. C., Vestergaard, M., Fan, X., Hopkins, P., Hernquist, L., Siemiginowska, A., 2010, ApJ 719:1315
 Kurk, J. D., et al., 2007, ApJ 669:32
 Kurk, J. D., Walter, F., Fan, X., Jiang, L., Jester, S., Rix, H. -W., Riechers, D. A., 2009, ApJ 702:833
 Nagao, T., Maiolino, R., Marconi, A., 2006, A&A 447:863
 Maiolino, R., Juárez, Y., Mujica, R., Nagar, N. M., Oliva, E., 2003, ApJ 596L:155
 Maiolino, R., Mannucci, F., Baffa, C., Gennari, S., Oliva, E., 2001, A&A 372L:5
 Matteucci, F., Recchi, S., 2001, ApJ 558:351
 McGill, K. L., Woo, J. -H., Treu, T., Malkan, M. A., 2008, ApJ 673:703
 McLure, R. J., Dunlop, J. S., 2004, MNRAS 352:1390
 McLure, R. J., Jarvis, M. J., 2002, MNRAS 337:109
 Pickles, A. J., 1998, PASP 110:863
 Peterson, B. M., 2010, IAUS 267:151
 Pentericci, L., Fan, X., Rix, H.-W., Strauss, M. A., Narayanan, V. K., Richards, G. T., Schneider, D. P., Krolik, J., 2002, AJ 123:2151
 Shang, Z., et al., ApJ 586:52
 Shen, Y., et al., 2010, arXiv1006.5178
 Shen, Y., Greene, J. E., Strauss, M. A., Richards, G. T., Schneider, D. P., 2008, ApJ 680:169
 Sigut, T. A. A., Pradhan, A. K., 2003, ApJS 145:15
 Spergel, D. N., et al., 2007, ApJS 170:377
 Venkatesan, A., Schneider, R., Ferrara, A., 2004, MNRAS 349L:43
 Vestergaard, M., Wilkes, B. J., 2001, ApJS 134:1
 Volonteri, M., 2010, A&ARv 18:279
 Volonteri, M., Rees, M. J., 2005, ApJ 633:624
 Willott C. J., et al., 2007, AJ 134:2435
 Willott, C. J., et al., 2010, AJ 140:546
 Willott C. J., Delorme P., Reylé C., Albert L., Bergeron, J., Crampton, D., Delfosse, X., Forveille, T., 2010, AJ 139:906
 Willott, C. J., McLure, R. J., Jarvis, M. J., 2003, ApJ 587L:15
 Wills, B. J., Netzer, H., Wills, D., 1985, ApJ 288:94
 Wyithe, J. S. B., Loeb, A., 2003, ApJ 595:614
 Xu, Y., et al., 2008, MNRAS 389:1703
 York, D. G., et al., 2000, AJ 120:1579

APPENDIX

FIT RESULTS: LITERATURE DATA

Hereafter we show the fit results for the literature sample and the relative χ^2 maps for Fe II error computation (analogous to Fig. 3.4). The sources are sorted in redshift.

In the right panels we show the spectral decomposition. The observed spectra are shown as a black continuous line. The modeled components are: power-law continuum (blue dotted line), Balmer pseudo continuum (purple dashed

line), Fe II normalized template (light blue dotted line), Mg II emission line (red dotted line). The sum of the first set of components (power-law continuum + Balmer pseudo continuum + Fe II normalized template) is overplotted to the spectrum as green solid line, while the sum of all the components is overplotted as a red solid line. Telluric absorption bands are indicated over the spectra with the symbol \oplus : they are extracted from the ESO sky absorption spectrum measured on the Paranal site at a nominal airmass of 1.

The Fe II normalization, obtained from the fit of the first set of components, depends on the power-law slope and its normalization (intercept). In the left panel we show the χ^2 domain analysis for Fe II error computation: a) two dimensional projections of the 3D χ^2 -surfaces (Fe II normalization vs Intercept, upper-left plot; Fe II normalization vs Slope, bottom-left plot; Intercept vs slope, bottom-right plot): contours represent iso- χ^2 levels spaced by a factor of 2 while the best fit case is marked with a dot; b) probability distribution for the Fe II template normalization (upper-right plot): the distribution has been obtained by marginalizing the 3-D probability distribution considering only the triplets for which $\chi^2 - \chi^2_{min} < 1$, the dashed vertical lines mark our estimate of the $1 - \sigma$ confidence level.

